Advances in Civil Engineering

RESEARCH ARTICLE OPEN ACCESS

Effects of Ferrous Slag Composition on Properties of Carbonated Ferrous Slag–Calcium Carbide Slag Brick

Weida Cao[1] | Quanbing Yang[2]

[1]Chengdu Huge Construction Material Co., Ltd., Chengdu 610041, China | [2]Key Laboratory of Advanced Civil Engineering Materials of the Ministry of Education, School of Material Science and Engineering, Tongji University, Shanghai 200092, China

Correspondence: Weida Cao (wdcao@163.com)

Received: 17 January 2026 | **Revised:** 10 June 2026 | **Accepted:** 24 June 2026

Academic Editor: Manoj Khandelwal

Keywords: brick | carbonation | ferrous slag | granulated blast furnace slag | steel slag

ABSTRACT

This study develops a carbonated ferrous slag–calcium carbide slag (FS-CCS) brick, carbonated under a simulated CO_2 concentration (~20%) representative of typical iron and steel industry waste gas. The influence of ferrous slag composition, that is, the proportions of steel slag (SS) and ground granulated blast furnace slag (GGBFS), on the performance of both carbonated and uncarbonated bricks was systematically investigated, along with the underlying carbonation mechanisms. The results indicate that carbonation enhances compressive strength by up to 281% (from 5.3 to 20.2 MPa for 100% SS mix), reduces water absorption by up to 21.5% (from 13.0% to 10.2% for 100% SS mix), improves volume stability, and completely resolves soundness issues. Increasing SS content amplifies the carbonation improvement on compressive strength and water absorption, but diminishes the improvement on drying shrinkage. The CO_2-sequestration rate of the carbonated brick rises with SS content, reaching 6.44% for the 100% SS mix. Microstructural analysis reveals that a higher SS content favors the pore-filling precipitation of $CaCO_3$ (a positive effect) over the decomposition of C–S–H (a negative effect), elucidating the observed performance trends. The optimal ferrous slag composition for the carbonated brick is 100% SS. The resulting product exhibits a compressive strength of 20.2 MPa, water absorption of 10.2%, dry shrinkage of 0.034% and eligible soundness, fully meeting the MU20 specifications for building bricks. Moreover, it is superior to conventional MU20 building brick available on the market due to its favorable properties, high CO_2-sequestration rate and high SS utilization rate. This makes it a viable candidate for nonload-bearing and low-load-bearing applications, including partition walls, pavement blocks, curbs, and so on, demonstrating its strong potential as a sustainable construction material derived from industrial by-products.

1 | Introduction

The iron and steel industry is a major contributor to global CO_2 emissions, responsible for 5%–7% of the total anthropogenic CO_2 released worldwide [1]. Several measures such as scrap steel recycling are, hence, being developed to cut its CO_2 emissions, but more drastic measures are required if reduction goals are to be met in a reasonable time frame [2]. Notably, a substantial portion of this CO_2 is discharged via the industry's waste gas, in which its concentration typically reaches around 20% [3]. Thus, directly capturing CO_2 from this gaseous effluent presents a clear pathway to reducing the carbon footprint of the iron and steel industry.

Concurrently, the iron and steel industry generates substantial quantities of ferrous slag, notably granulated blast furnace slag (GBFS, 25–30 wt% of crude steel output) and steel slag (SS, 10–15 wt% of crude steel output) [1]. GBFS is a glassy calcium-

This is an open access article under the terms of the Creative Commons Attribution License, which permits use, distribution and reproduction in any medium, provided the original work is properly cited.

Copyright © 2026 Weida Cao and Quanbing Yang. *Advances in Civil Engineering* published by John Wiley & Sons Ltd.

aluminum silicate coproduct produced during the blast furnace iron-making process [4]. Due to its high glass phase content, GBFS serves as a popular precursor for the alkali-activated materials [5, 6] and is widely utilized in China for cement and concrete production. In contrast, SS is generated during the steelmaking process, predominately as basic oxygen furnace slag [7, 8]. Although the chemical and mineral composition of SS resembles that of cement, its low activity and poor soundness, caused by the low reactivity of the silicate mineral phase (C_2S and C_3S) and the presence of f-CaO, hinder its utilization [9]. As a result, only 20% SS is reused in China, most SS is in the state of disuse and haphazard accumulation [10], leading to environmental pollution, land occupation, and resource wastage. Therefore, resource utilization of SS is urgently needed.

Owing to its good physical properties [11], SS could be used as an aggregate to enhance the mechanical performance of concrete [12–14]. However, because of soundness concerns, SS aggregate requires an aging or weathering process prior to use. Due to its C_2S and C_3S content, SS also exhibits potential hydraulic activity and has been activated by high-temperature [15, 16], mechanical [17], and alkali excitation [18–21]. Nevertheless, although the mechanical performance of activated SS–based materials shows some improvement, it remains poor, suggesting that SS may not be an ideal precursor for activation [22]. Moreover, as a result of its high CaO and MgO content (34%–52%) [23], SS is also considered a potential feedstock for CO_2 sequestration. To maximize the CO_2 uptake, SS is often leached prior to CO_2 sequestration [24–27]. Nonetheless, despite achieving a high CO_2 sequestration rate (above 200 kg CO_2/t SS), this approach fails to address residual slag after leaching, leaving the issue of SS disposal unresolved. Therefore, a more comprehensive and sustainable recycling method should be explored.

On the other hand, rapid urbanization in China has driven an enormous demand for building bricks. According to the statistics [28], 210 billion building bricks, primarily solid concrete bricks and fired common bricks, were produced in China in 2023, widely used in partition walls, pavements, landscaping, and curbs. Although solid wastes, including mine tailing, recycled aggregate, bottom ash, and so on [29] have been utilized in brick production, conventional materials like cement, sand, and clay are still required to achieve adequate performance. Moreover, fuel energy consumption remains inevitable during brick manufacturing, particularly for fired common bricks [30]. Consequently, given the huge volume of brick production in China, substantial natural and energy resources are consumed, highlighting the urgent need for a sustainable alternative to building bricks.

Considering the substantial CO_2 emissions and massive ferrous slag output of the iron and steel industry, utilizing these waste streams to produce building bricks presents an efficient, green, and economical route for large-scale recycling, given the vast market demand for building bricks in China. Wu et al. [31] prepared a high-strength building material with eligible soundness by carbonating a compacted steelmaking slag mixture with pure and pressurized CO_2. Xu et al. [32] fabricated a carbonated SS slab with a maximum strength of 232 MPa via a compacting process and accelerated carbonation. Biava et al. [33] converted SS into a pozzolanic cementitious material through NaOH pretreatment, followed by carbonation with pure CO_2. Liu et al. [34] reported a carbonated fine SS powder–cement–based mortar via ambient carbonation curing (298 K, 0.2 CO_2 atm, 1 bar, and 65% RH). This mortar exhibits a compressive strength of 31.2 MPa and uptakes CO_2 nearly 80 kg/m^3. These technologies incorporate ferrous slag and CO_2 into building materials, but their reliance on compaction, pure and pressurized CO_2, and cement clinker significantly compromises their practical applicability, sustainability, and cost-effectiveness.

Recent researches [35–38] report that calcium carbide slag (CCS), a $Ca(OH)_2$-rich byproduct of calcium carbide production, is able to alkali activate ferrous slag. Meanwhile, thanks to its high $Ca(OH)_2$ content, CCS is also considered an ideal feedstock for CO_2 sequestration. Accordingly, investigations on carbonation of the ferrous slag–CCS (FS-CCS) mixture have been carried out. Zhang et al. [39] prepared a building material by carbonating a composite of CCS and GBFS via ambient carbonation curing (CO_2 20% and RH 65%). The resulting carbonated mixture with 30%CCS and 70%BFS exhibits strength of 15.5 MPa after 28 carbonation curing. This technology enables the reuse of GBFS, CCS, and CO_2, presenting a sustainable alternative to building bricks. Nevertheless, as GBFS is its main raw material, this technology does not resolve the SS disposal problem. Thereby, alternative strategies are required.

To address the disposal problem of ferrous slag from the iron and steel industry, especially SS, this study employs ground granulated blast furnace slag (GGBFS) and SS as base materials and CCS as an alkali activator to prepare a composite mixture. This mixture is then carbonated under a CO_2 concentration similar to that of waste gas from the iron and steel industry, producing a novel building brick, that is, carbonated FS-CCS brick. This novel product is not only derived entirely from waste but also offers a feasible pathway for direct mitigating industrial CO_2 emissions, providing a sustainable and economical alternative to conventional building bricks.

Although both GGBFS and SS are ferrous slag from the iron and steel industry, they are fundamentally different in terms of production, chemistry, and phase assemblage and consequently exert different effects on the alkali activation and carbonation. Given that alkali activation and carbonation are the key processes in producing this carbonated brick, understanding these effects is essential prior to practical application. Hence, this study aims to systematically assess the effects of ferrous slag composition, that is, the proportions of SS and GGBFS, on the properties of carbonated FS-CCS bricks and the efficacy of the carbonation process, as well as the underlying mechanism. The properties measured include compressive strength, water absorption, soundness, drying shrinkage, and CO_2-sequestration rate.

2 | Experiments

2.1 | Raw Materials

SS and GGBFS supplied by Bao Steel Co., Ltd. were used as base materials in this study. The SS is a basic oxygen furnace slag with a specific surface area of 450 m^2/kg and a density of 3290 kg/m^3. The GGBFS has a specific surface area of 420 m^2/kg and a density of 2870 kg/m^3. CCS from Tianyuan Chemical Co., Ltd. with 20% moisture content was used as an alkali activator. On a dry basis, CCS has a specific surface area of 360 m^2/kg and a density of

TABLE 1 | Chemical composition of the raw materials (wt%).

Raw materials	SiO_2	Al_2O_3	CaO	MgO	TiO_2	MnO	Fe_2O_3	SO_3	LOI
SS	12.12	4.72	40.61	10.34	0.76	2.52	17.09	0.17	2.1
GGBFS	32.99	14.62	40.22	7.77	0.47	0.40	2.29	0.14	0.16
CCS[a]	1.74	1.03	70.58	1.70	–	–	0.21	–	23.03

[a]CCS is on a dry mass.

2100 kg/m^3. The chemical compositions of these materials are summarized in Table 1.

River sand, with a fineness modulus of 2.76 and a bulk density of 1140 kg/m^3, was used as the aggregate. It can be replaced by GBFS and mining tails for economic and environmental concerns. To simulate the carbonation conditions similar to the iron and steel industry waste gas, an environment with approximately 20 % CO_2 concentration was established using pure CO_2 supplied by Air Liquide.

2.2 | Sample Preparation

Five mix proportions by varying the ferrous slag composition are given in Table 2. Their CCS/ferrous slag (GGBFS + SS) ratio, water/binder (CCS + ferrous slag) ratio, and sand/binder ratio were kept constant at 0.2, 0.5, and 2.0, respectively, as these mix proportions resulted in carbonated brick with adequate compressive strength and acceptable carbonation duration.

The raw materials were mixed and cast into molds of 40 mm × 40 mm × 160 mm. All samples were demoulded after 72 h curing at 60 ± 5%rh and 20 ± 5°C and then underwent steam curing at 50 ± 5°C for 24 h to enhance their early strength for further handling and testing. After cooling, half of the samples were fully carbonated in carbonation equipment with a CO_2 concentration of 20% ± 1%, 60 ± 1%rh, and 20 ± 5°C for 8 days to prepare the carbonated FS-CCS brick. The other half was stored in an environment with 20 ± 5°C and 60 ± 1%rh for the same duration to prepare the uncarbonated FS-CCS brick as a comparison.

To further investigate the mechanism and the CO_2-sequestration rate, parallel carbonated and uncarbonated FS-CCS pastes without aggregate were prepared following the same procedures. Their mix proportions are listed in Table 2.

TABLE 2 | Mix proportions (kg·m^{-3}).

Mix		GGBFS	SS	CCS[a]	Aggregate	Water
Brick	A	525	0	105	1260	315
	B	394	131	105	1260	315
	C	263	262	105	1260	315
	D	131	394	105	1260	315
	E	0	525	105	1260	315
Paste	AP	525	0	105	0	315
	CP	263	262	105	0	315
	EP	0	525	105	0	315

[a]CCS is measured by dry mass.

2.3 | Test Methods

The mechanical and physical properties of the brick, including compressive strength, water absorption, and drying shrinkage, were measured in accordance with GB/T 2542-2012: Test Methods for Wall Bricks [40]. The soundness of the brick was tested in accordance with GB/T750-2024: soundness of Portland Cement [41]. The specific test methods are as follows:

1. Compressive strength was determined at a loading rate no more than 2 N·mm^{-2}·s^{-1}.
2. Drying shrinkage was characterized by immersing the brick in water at 20 ± 5°C for 4 days (saturated state), then oven drying at 100 ± 5°C for 24 h (oven-dry state), and calculating the length change before and after oven drying (to eliminate the variations due to initial moisture).
3. Water absorption was measured by drying the brick at 80 ± 5°C for 48 h, cooling it to the room temperature in the vacuum desiccator, then immersing it in water at 20 ± 5°C for 24 h, and finally calculating the weight change before and after immersion.
4. Soundness was accessed by autoclaving the brick at 215 ± 2°C for 3 h. Brick exhibiting cracks or an expansion rate exceeding 0.8% was considered to have a soundness issue.

The mineralogical composition of the paste was identified by an X-ray powder diffractometer (XRD; AXS D8 ADVANCE, Bruker) with Cu Kα radiation at 35 kV and 40 mA. The differential thermal and thermogravimetric analysis (DTA/TG) of the paste was determined by using a Simultaneous Thermal Analysis Meter (STA449C, NETZSCH) with alumina crucibles, at 20°C·min^{-1} heating rate, under a static N_2 atmosphere. The microstructure of the paste was observed with environmental scanning electron microscope (ESEM; 200 FEG, FEI Quanta) at 30 kV and 2 μa in the vacuum environment. The pore structure analysis of the paste, including the surface area and the mesopore distribution, was determined by the Brunauer–Emmett–Teller method (BET; ASAP 2020, Micromeritics), while its porosity was calculated according to Equation (1) specified in ISO5017-2025 [42].

$$\pi_t = \frac{\rho_t - \rho_b}{\rho_t} \times 100, \quad (1)$$

where π_t, the porosity, %; ρ_t, the theoretical density, kg·m^{-3}; ρ_b, the bulk density, kg·m^{-3}.

3 | Results and Discussion

3.1 | Strength

Figure 1 presents the evolution of compressive strength of carbonated and uncarbonated FS-CCS bricks with varying SS

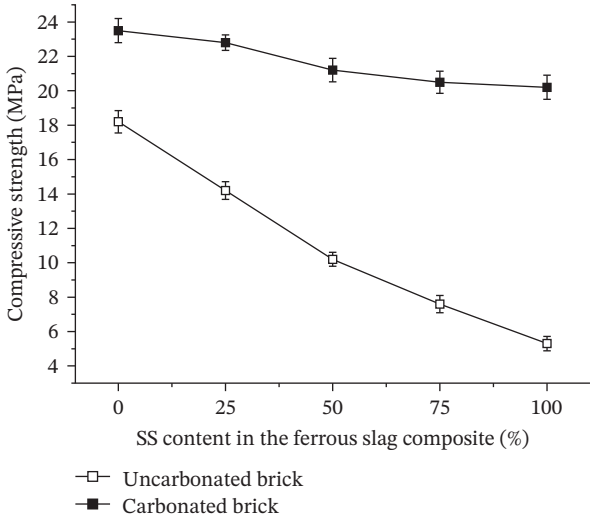


FIGURE 1 | Effects of the ferrous slag composition on the compressive strength of the carbonated and uncarbonated FS-CCS bricks.

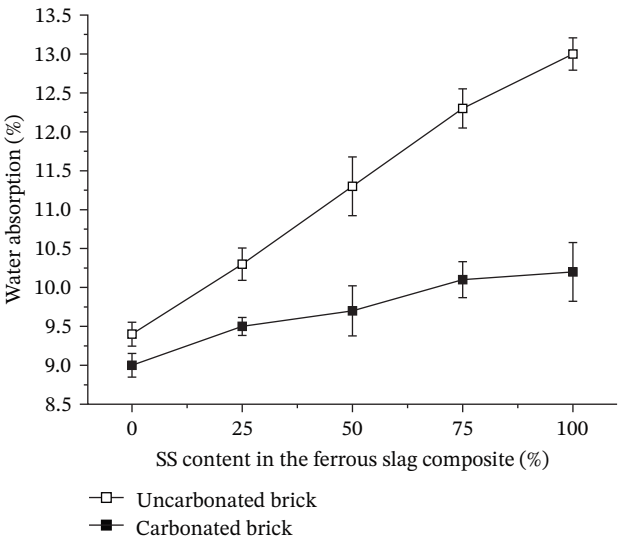


FIGURE 2 | Effects of the ferrous slag composition on the water absorption of the carbonated and uncarbonated FS-CCS bricks.

content. As shown in Figure 1, with increasing SS content, the compressive strength of the uncarbonated brick decreases with statistical significance. In contrast, the compressive strength of the carbonated one declines slightly, and the differences between certain SS contents (0% vs. 25% and 75% vs. 100%) are not statistically significant. For example, when the SS content increases from 0% to 100%, the compressive strength of the uncarbonated brick drops from 18.2 to 5.3 MPa, with a reduction of 70.9%, while that of the carbonated one decreases from 23.5 to 20.2 MPa, with a reduction of 14.0%. Furthermore, all carbonated bricks exhibit higher strength than their uncarbonated counterparts. Specifically, at 0% SS content, that is, 100% GGBFS, the carbonated brick shows a 29% higher strength; at 100% SS content, it shows a 281% higher strength. Results indicate that SS substantially reduces the strength of uncarbonated brick but has a minor effect on the carbonated one. Furthermore, carbonation increases the strength of the carbonated brick, and this strengthening effect becomes pronounced with a higher SS content. This finding is similar to the results presented in previous studies [34, 43, 44], which reported that carbonation products are able to densify the microstructure, thereby enhancing the strength of ferrous slag–based materials by 200%–300%. However, the late-strength decline caused by carbonation, as reported by Zhang et al. [39], was not observed in this study. This negative effect has been ascribed by the authors to the microcracks resulting from the volume expansion of carbonation products.

3.2 | Water Absorption

Figure 2 presents the evolution of water absorption of the carbonated and uncarbonated FS-CCS bricks with varying SS content. As shown in Figure 2, with increasing SS content, the water absorption of the uncarbonated brick increases with statistical significance. In contrast, the water absorption of the carbonated one rises modestly, and the differences between certain SS contents (25% vs. 50% and 75% vs. 100%) are not statistically significant. For instance, when the SS content increases from 0% to 100%, the water absorption of the uncarbonated brick escalates from 9.4% to 13.0%, with an increment of 38.3%, while that of the carbonated one grows from 9.0% to 10.2%, with an increment of 13.3%. Notably, all carbonated bricks exhibit lower water absorption than their uncarbonated counterparts. Specifically, at 0% SS content, the carbonated brick exhibits 4.2% lower water absorption, while it shows 21.5% lower water absorption at a 100% SS content. Results indicate that SS increases the water absorption in both carbonated and uncarbonated brick, with the effect being pronounced in the uncarbonated brick. Furthermore, carbonation reduces the water absorption of the carbonated brick, and this reducing effect becomes pronounced with a higher SS content. This finding aligns with the results achieved in the work of Zhang et al. [45], which reported that carbonation is able to lower the water absorption of SS concrete by nearly 20%, an effect the authors attributed to the porosity reduction caused by carbonation.

3.3 | Drying Shrinkage

Figure 3 presents the evolution of drying shrinkage of the carbonated and uncarbonated FS-CCS bricks with varying SS content. As shown in Figure 3, with increasing SS content, the drying shrinkage of the uncarbonated brick decreases significantly. In contrast, the drying shrinkage of the carbonated one shows only a marginal decline, which is not statistically significant. For instance, when the SS content increases from 0% to 100%, the drying shrinkage of the uncarbonated brick drops from 0.128% to 0.077%, with a reduction of 39.8%, while that of the carbonated one decreases from 0.045% to 0.034%, with a reduction of 24.4%. Moreover, all carbonated bricks exhibit lower drying shrinkage than their uncarbonated counterparts. Specifically, at 0% SS content, the carbonated brick exhibits a 64.0% lower shrinkage, while at 100% SS content, it shows a 55.8% lower shrinkage. Results indicate that SS substantially reduces the drying shrinkage of the uncarbonated brick but has only a minor effect on the carbonated one. Furthermore, carbonation mitigates the drying shrinkage of the carbonated brick, and this mitigating effect diminishes with a higher SS content. This finding is supported by the results presented in Liu et al.'s [46] study, which reported that carbonation improves the volume stability of SS concrete by mitigating 80% of its volume deformation. The authors ascribed such improvement to an increase in moisture and the formation of carbonation products.

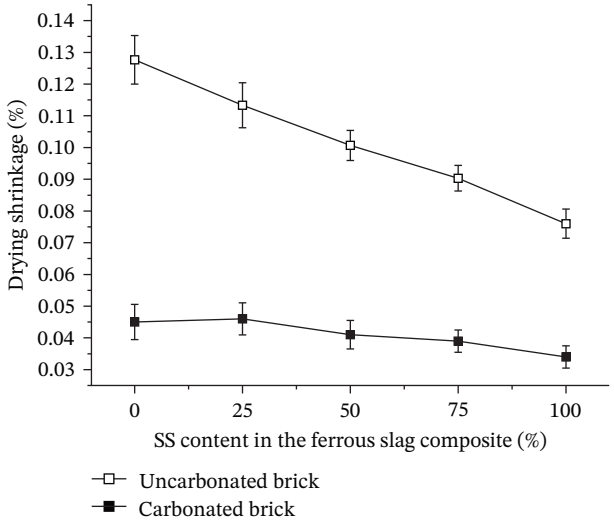


FIGURE 3 | Effects of the ferrous slag composition on the dry shrinkage of the carbonated and uncarbonated FS-CCS bricks.

3.4 | Soundness

The autoclaving soundness test results for the carbonated and uncarbonated FS-CCS bricks with varying SS content are summarized in Table 3. As shown in Table 3, except for Mix A and B, the uncarbonated bricks exhibit unacceptable soundness, and their soundness performance deteriorates with increasing SS content. In contrast, all the carbonated bricks demonstrate eligible soundness as they remain intact and show volume expansions far below the limit (≤0.8%) after autoclaving [41]. Results indicate that the soundness issue of the uncarbonated brick originates from the SS and can be completely eliminated by carbonation. This finding is consistent with previous studies [31, 45, 47], which ascribe this improvement to the carbonation of f-CaO and f-MgO in SS.

3.5 | CO_2-Sequestration Rate

In the carbonated FS-CCS brick, CO_2 is sequestered through the reaction of the FS-CCS mixture, that is, the carbonated FS-CCS paste, with CO_2 to form carbonates. Consequently, the mass loss from the de-carbonation of these carbonates in the carbonated paste is equivalent to the mass of CO_2 sequestered in the corresponding brick. Therefore, the CO_2 sequestration rate of the carbonated brick can be calculated by using Equation (2).

$$E_m = \frac{R_{\text{loss}}}{(1 - R_{\text{loss}})(1 + S_r)}, \tag{2}$$

where E_m is the CO_2-sequestration rate of the carbonated brick, %; R_{loss} is the mass loss due to the decomposition of the carbonates in the carbonated paste, %; S_r is the sand/binder ratio.

Figure 4 presents the DTA/TG curves of the carbonated pastes. As shown in Figure 4a, the DTA curves show an endothermic peak at about 700–850°C, corresponding to the decomposition of $CaCO_3$ [48]. As measured from the TG curves (Figure 4b), the mass loss in carbonated AP, CP, and EP is 10.0%, 12.5%, and 16.5%, respectively. According to Equation (2), the CO_2-sequestration rate of carbonated brick A, C, and E is 3.70%, 4.76%, and 6.44%, respectively. Results indicate that the CO_2 sequestration rate of the carbonated brick increases with the SS content.

TABLE 3 | Results of the soundness test on the carbonated and uncarbonated FS-CCS bricks.

	Uncarbonated brick		Carbonated brick	
Mix	State	Expansion rate (%)	State	Expansion rate (%)
A	Intact	0.033 ± 0.004	Intact	0.014 ± 0.001
B	Intact	0.121 ± 0.010	Intact	0.018 ± 0.002
C	Crack	—	Intact	0.028 ± 0.003
D	Crack	—	Intact	0.028 ± 0.004
E	Fracture	—	Intact	0.025 ± 0.003

3.6 | Mechanism

The experimental results presented above demonstrate that carbonation effectively improves the properties of the carbonated FS-CCS brick, with the ferrous slag composition playing a significant

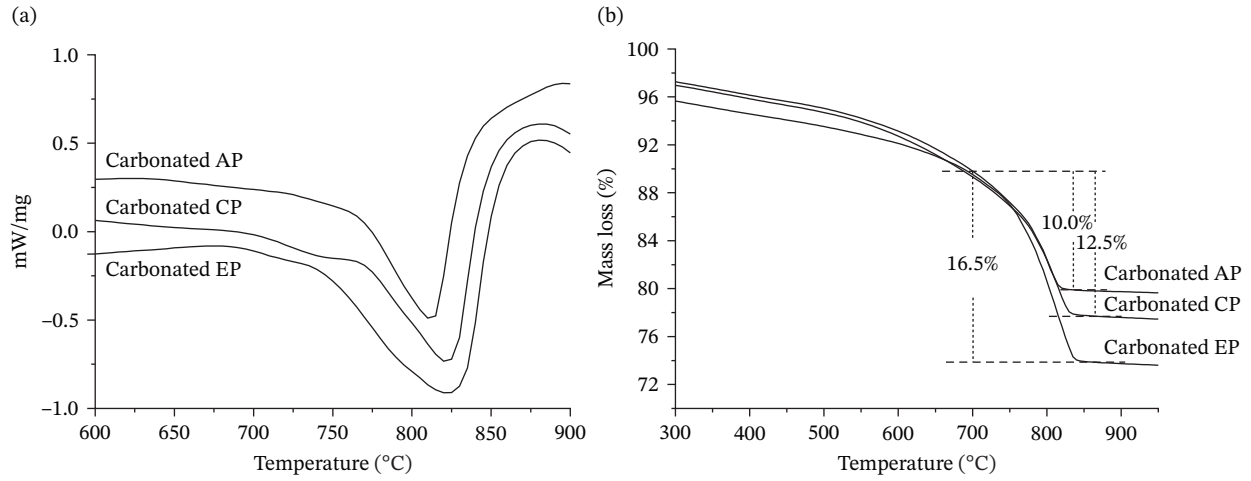


FIGURE 4 | DTA/TG curves of the carbonated FS-CCS pastes: (a) DTA curves and (b) TG curves.

role in the extent of these improvements. To elucidate the underlying mechanisms, the mineral composition, pore structure, and microstructure of both carbonated and uncarbonated FS-CCS pastes with varying ferrous slag composition were examined.

3.6.1 | Mineral Composition

Figure 5 presents the XRD patterns of SS, GGBFS, CCS, and carbonated and uncarbonated FS-CCS pastes. It shall be noted that because of the presence of Fe in the samples, microabosorption effects are expected during XRD measurements [49].

As shown in Figure 5a, SS is mainly consisted of C_2S, C_3S, iron oxides C_2F ($Ca_2Fe_2O_5$), and the RO phase (FeO/MnO). Since C_2S and C_3S in SS are well crystallized in a slow cooling process [50] and are wrapped by an inert phase [51], the activity of SS is rather low. Furthermore, it should be noted that SS also contains f-CaO, which leads to volume instability [9], as confirmed by the soundness test results in Table 3. Additionally, the presence of small amounts of $Ca(OH)_2$ and $CaCO_3$ indicates that it was moderately weathered and partially carbonated. In contrast, the GGBFS consists predominantly of a glass phase. Given its CaO/SiO_2 ratio of about 1.22 (Table 1), this glass phase is metastable [4], endowing GGBFS with high potential hydraulic activity. Additionally, CCS is mainly composed of $Ca(OH)_2$, along with a small amount of $CaCO_3$ resulting from the carbonation process.

After the activation by CCS, the peaks of $Ca(OH)_2$ become distinct in the uncarbonated pastes, as shown in Figure 5b. The peaks of C–S–H are visible in the uncarbonated paste AP and CP but are absent in EP. Additionally, the intensity of $Ca(OH)_2$ peaks increases with the SS content, indicating a corresponding rise in the $Ca(OH)_2$ content.

After carbonation, the peaks of $Ca(OH)_2$ and C–S–H disappear in the carbonated pastes, as shown in Figure 5c, while those of calcite-type $CaCO_3$ become much more intense. Notably, vaterite-type $CaCO_3$ is detected in the carbonated pastes AP and CP. Furthermore, the intensity of the peaks of calcite-type $CaCO_3$ increases with the SS content, suggesting that the $CaCO_3$ content rises accordingly.

3.6.2 | Pore Structure

Table 4 and Figure 6 present the pore structure analysis on the carbonated and uncarbonated FS-CCS paste. As summarized in Table 4, the carbonated pastes exhibit lower porosity than their

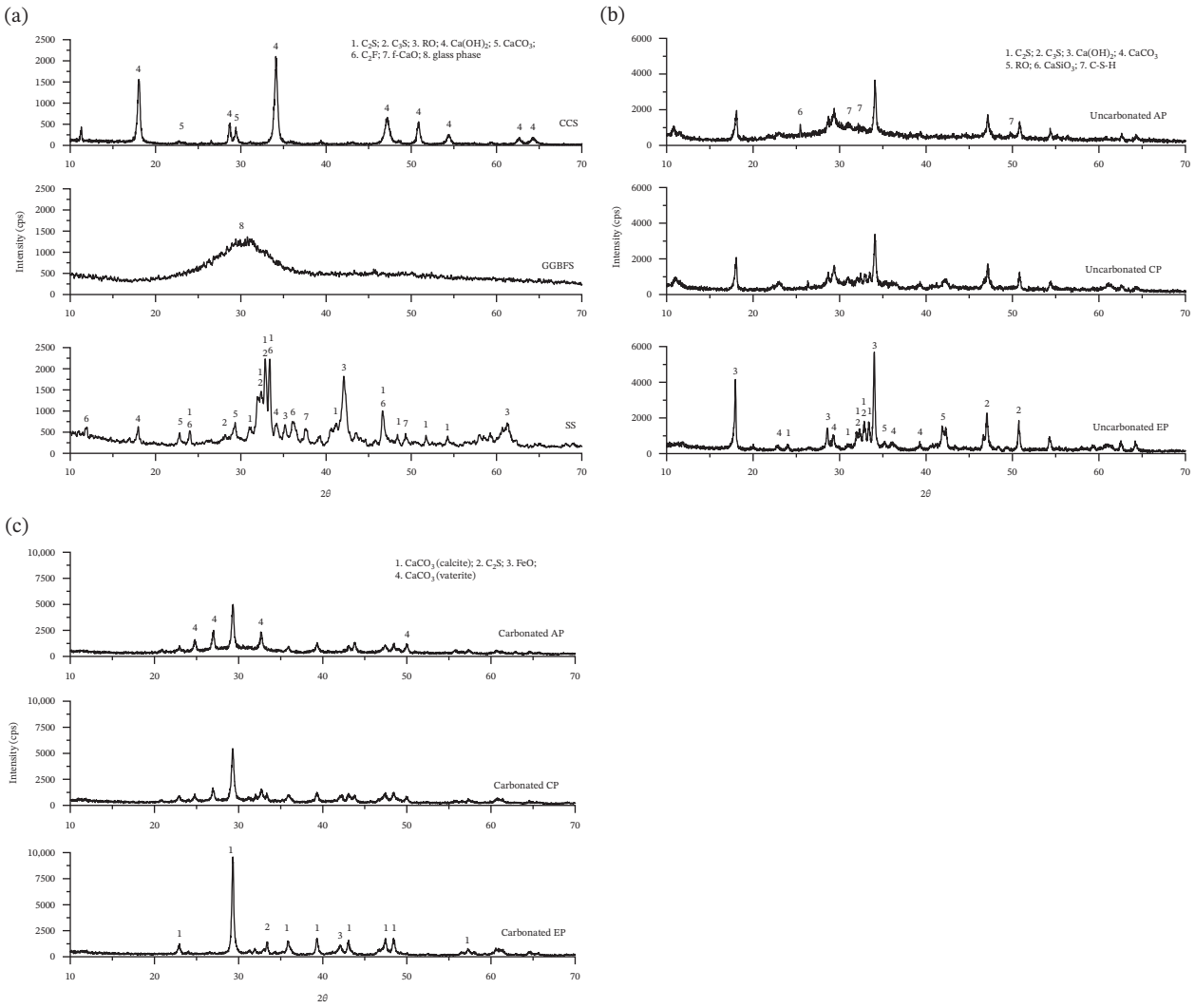


FIGURE 5 | Mineralogical compositions of steelmaking slags, carbonated and uncarbonated FS-CCS pastes: (a) GGBFS, SS, and CCS; (b) uncarbonated pastes; (c) carbonated pastes.

TABLE 4 | The pore structure analysis on carbonated and uncarbonated SmS-CS paste.

Sample		True porosity (%)	Specific Surface area ($m^2 \cdot g^{-1}$)
Uncarbonated paste	AP	35.2	8.63
	CP	40.7	7.34
	EP	50.9	4.59
Carbonated paste	AP	30.8	6.33
	CP	32.9	5.98
	EP	35.3	3.89

uncarbonated counterparts. Furthermore, with increasing SS content, the porosity of the uncarbonated pastes rises significantly, whereas that of the carbonated pastes grows marginally.

As shown in Figure 6a, the uncarbonated pastes contain two distinct populations of mesopores: small mesopores (3–4 nm) and large mesopores (12–50 nm). The large mesopores constitute the majority of the mesopore volume, and their volume decreases as the SS content increases. In contrast, the carbonated pastes contain only small mesopores and show little change in mesopore volume with increasing SS content (Figure 6b). Furthermore, it is noteworthy that the total mesopore volume in the carbonated pastes is lower than that in the uncarbonated ones.

Table 4 further summarizes the specific surface area of the carbonated and uncarbonated paste. As listed in Table 4, the specific surface area of both carbonated and uncarbonated pastes decreases with increasing SS content. Furthermore, carbonation reduces the specific surface area of the carbonated pastes, and this reduction becomes more pronounced at higher SS contents.

As mentioned above, both the incorporation of SS and the carbonation process reduce the mesopore volume and specific surface area of the pastes. Since C–S–H is the primary mesoporous phase and possesses a high surface area [52], these observations suggest that both the incorporation of SS and the carbonation process reduce the overall C–S–H content in the paste. These findings are consistent with the XRD analysis results.

3.6.3 | Microstructure

Figure 7 presents ESEM images of carbonated and uncarbonated SmS-CS paste (EP). As shown in Figure 7b, hydration product C–S–H and hexagonal plate-shaped portlandite are observed in the uncarbonated paste. Additionally, numerous macropores are clearly visible in the uncarbonated paste, indicating a porous microstructure (Figure 7a). These observations confirm that the uncarbonated paste is porous, with high porosity and total pore volume, which is consistent with BET results presented in Table 4 and Figure 6.

After carbonation, as shown in the ESEM image of the carbonated paste (Figure 7d), the hexagonal plate-shaped portlandite disappears and is replaced by abundant cubic calcite crystals. Notably, macropores in the carbonated paste are fewer and less distinct, suggesting a dense microstructure (Figure 7c). Consequently, the carbonated paste exhibits low porosity and total pore volume, as verified by the BET results presented in Table 4 and Figure 6.

3.6.4 | Discussion

Based on the experimental results of this study, it is believed that CCS is capable of activating the hydration of both GGBFS and SS. In the case of GGBFS, CCS creates an alkali environment through its hydrolysis and thereby promotes the dissolution of glassy aluminiumsilicate in GGBFS. The chemical bonds in the silica-oxygen tetrahedral and alumina–oxygen tetrahedral break, releasing numerous SiO_4^{2-} and AlO_4^{5-}, which react with $Ca(OH)_2$ (from CCS) to form C–(A)–S–H [53, 54], that is, the pozzolanic reaction of GGBFS occurs. In the case of SS, CCS erodes the inert phase on the surface of SS particles, exposing the reactive C_2S and C_3S inside [51] and promoting their hydration, which generates C–S–H and $Ca(OH)_2$ [50].

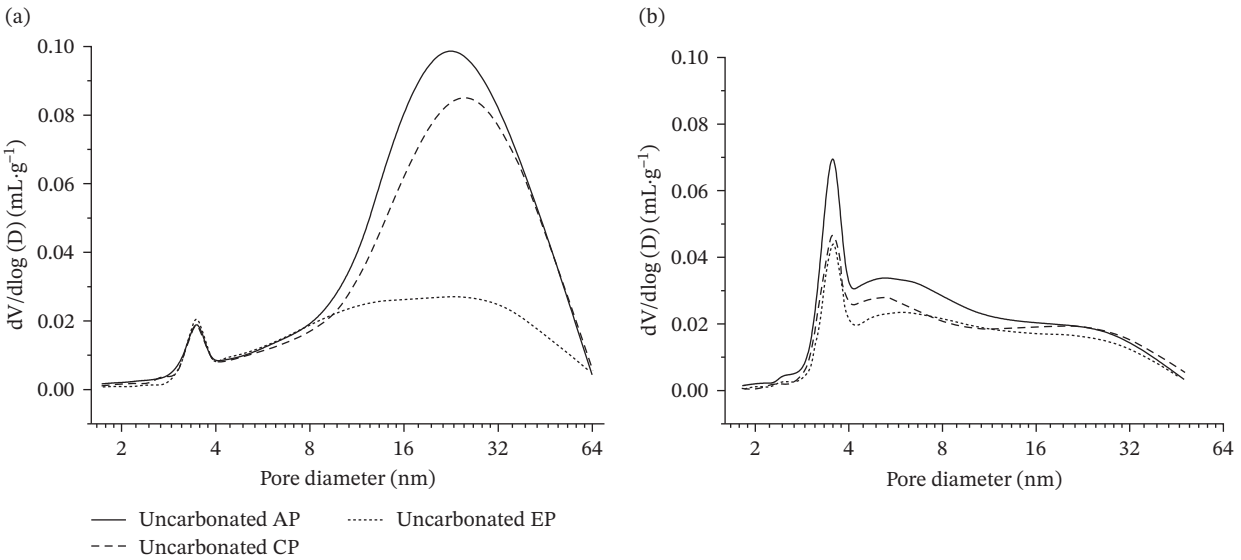


FIGURE 6 | The differential curves of mesopore-size distribution of uncarbonated and carbonated FS-CCS paste: (a) uncarbonated pastes and (b) carbonated pastes.

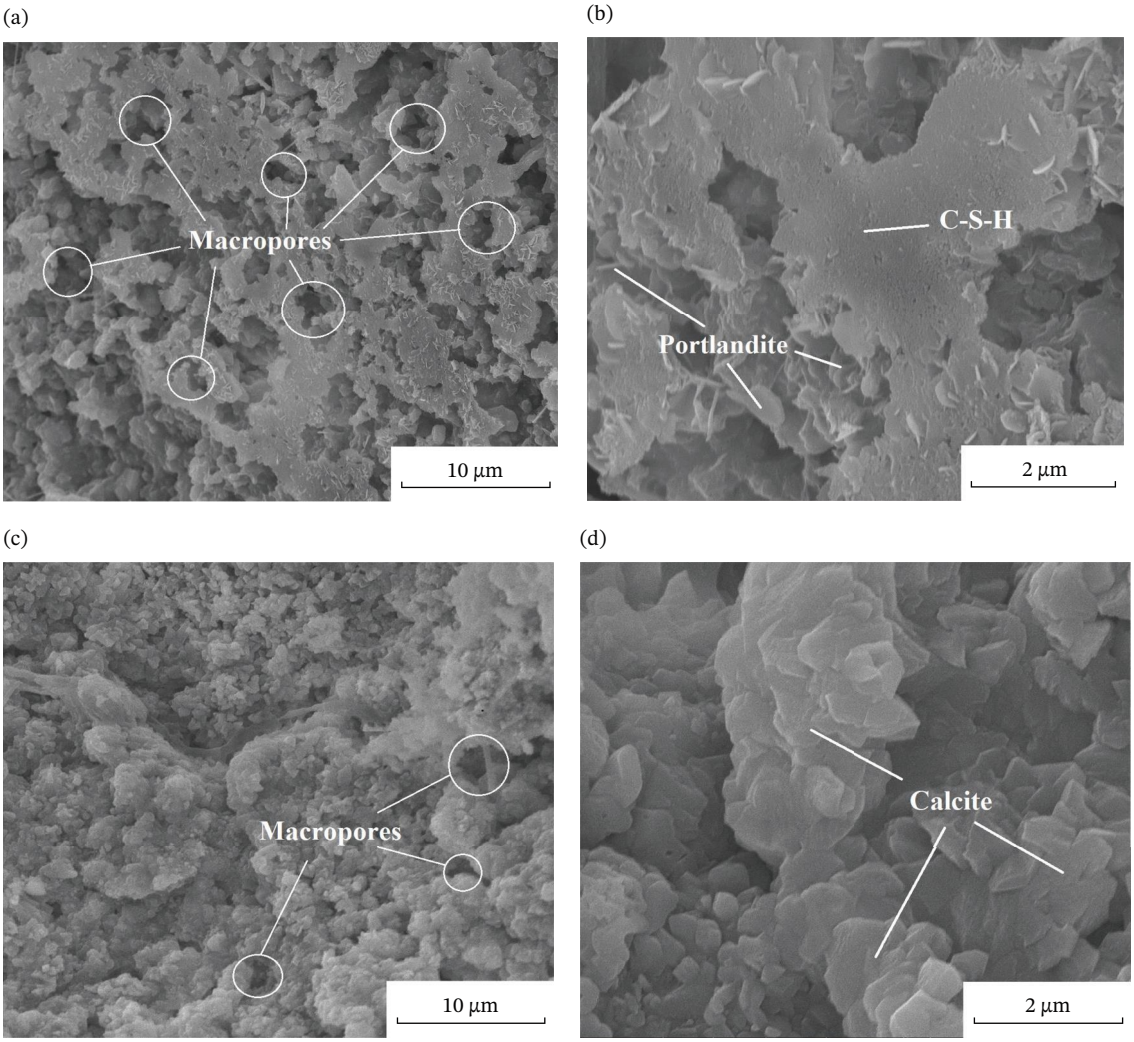


FIGURE 7 | The ESEM image of uncarbonated and carbonated FS-CCS paste EP: (a) uncarbonated pastes, 5000× magnification; (b) uncarbonated pastes, 30,000× magnification; (c) carbonated pastes, 5000× magnification; (d) carbonated pastes, 30,000× magnification.

Evidently, owing to its high pozzolanic reactivity, GGBFS consumes more $Ca(OH)_2$ (from CCS) for activation during hydration and produces more C–S–H. In contrast, due to the dense inert phase on SS particles, less $Ca(OH)_2$ (from CCS) is consumed to activate SS. Besides, the hydration of C_2S and C_3S in SS also generates additional $Ca(OH)_2$ as a hydration product. Meanwhile, because of their high crystallinity, C_2S and C_3S in SS exhibit low reactivity, resulting in less C–S–H formation during SS hydration. Therefore, with increasing SS content, the $Ca(OH)_2$ content in the uncarbonated brick rises, whereas the C–S–H content declines, as evidenced by the specific surface area results in Table 4.

Since hydration product C–S–H serves as the primary binder in the uncarbonated brick, increased SS content leads to lower C–S–H content and consequently a more porous microstructure (Figure 7a; Table 4), thereby reducing its compressive strength and increasing water absorption. This trend is verified by the evolution of compressive strength and water absorption of uncarbonated brick with varying SS content (Figures 1 and 2). Furthermore, as C–S–H is also considered the main contributor to drying shrinkage due to its mesoporous structure, where water evaporation induces capillary stresses and causes contraction [55, 56], increasing SS content results in lower C–S–H content in the uncarbonated brick and consequently reduces drying shrinkage. This trend is confirmed by the drying shrinkage evolution of uncarbonated bricks with varying SS content (Figure 3). Additionally, because of the presence of f-CaO in SS, as confirmed by XRD (Figure 5a), the soundness issues of the uncarbonated brick become more severe with increasing SS content. This explains the soundness evolution of uncarbonated bricks with varying SS content (Table 4).

Upon carbonation, $Ca(OH)_2$ (from CCS and the hydration product of SS) is converted into calcite-type $CaCO_3$. Since CO_2 diffuses into the brick through pores and capillaries and because the molar volume of calcite-type $CaCO_3$ is approximately 11.8% larger than that of $Ca(OH)_2$ [57], the newly formed calcite-type $CaCO_3$ precipitates within the pores and gradually fills them. This process reduces pore volume and densifies the microstructure of the carbonated brick, as evidenced by the porosity results in Table 4, leading to higher strength and lower water absorption compared to the uncarbonated one. This is confirmed by the comparative data on compressive strength and water absorption (Figures 1 and 2). Conversely, carbonation also decomposes C–S–H into vaterite-type $CaCO_3$ [58] and silica gel [59], as supported by XRD (Figure 5c) and the BET results in Table 4. Since C–S–H serves as the primary binding phase, its decomposition inevitably weakens the carbonated brick, potentially impairing its properties.

TABLE 5 | The properties of the carbonated FS-CCS brick and MU20 building brick available in the market.

Building brick		Properties		
		Compressive strength (MPa)	Water absorption (%)	Drying shrinkage (%)
MU20 solid concrete brick	GB/T21144-2023 [60]	≥20	≤11.0	≤0.05
	Shengjing Co., Ltd.	21.9	6.8	0.065
	Suborui Building materials Co., Ltd.	22.2	5.9	0.055
MU20 fired common brick	GB5101-2017 [61]	≥20	≤16.0	–
	Shutao new materials Co., Ltd.	21.5	14.3	–
	Jianyuan Construction Materials Co., Ltd.	20.5	15.5	–
MU20 nonfired brick with solid waste and tailing	JC/T422-2025 [62]	≥20	≤15.0	≤0.06
	Sanhe green building materials Co., Ltd.	20.2	11.9	0.058
Carbonated FS-CCS brick		20.2	10.2	0.034

Hence, carbonation exerts two competing effects on the carbonated brick: a positive effect by pore-filling with newly formed $CaCO_3$ and a negative effect by C–S–H decomposition.

As SS consumes less $Ca(OH)_2$ and produces less C–S–H than GGBFS, a higher SS content yields lower initial C–S–H content but higher $Ca(OH)_2$ content in the uncarbonated brick. Consequently, during carbonation, less C–S–H is available for decomposition, whereas more $CaCO_3$ precipitates. This shift amplifies the positive pore-filling effect of $CaCO_3$ and attenuates the negative effect of C–S–H decomposition. As a result, the improvement in compressive strength and water absorption achieved through carbonation becomes increasingly pronounced at a higher SS content. This explains the evolution of the carbonation effect on these properties with varying SS content (Figures 1 and 2). Similarly, as mentioned earlier, carbonation decomposes mesoporous C–S–H, the main cause of shrinkage, into vaterite-type $CaCO_3$ and silica gel. Although silica gel may retain some mesoporosity, its proportion is substantially lower than that of $CaCO_3$ (including calcite-type and vaterite-type), which exhibits excellent volume stability. For this reason, carbonation effectively improves the volume stability of the carbonated brick, as confirmed by the comparative drying shrinkage data (Figure 3). Consequently, a higher initial C–S–H content in the uncarbonated brick leads to more extensive decomposition during carbonation and results in a more pronounced improvement on volume stability, which explains the evolution of carbonation effect on the drying shrinkage with varying SS content (Figure 3). Furthermore, since CO_2 sequestration of the carbonated brick depends primarily on the carbonation of $Ca(OH)_2$, a higher $Ca(OH)_2$ content leads to a greater CO_2 uptake. Therefore, the CO_2 sequestration rate of the carbonated brick increases with the SS content, which explains the observed trend in Figure 4. Finally, by converting f-CaO in SS into stable $CaCO_3$, carbonation eliminates the soundness issue, resulting in a sound-carbonated product, as verified by the soundness test results (Table 3).

4 | Comparative Analysis of Carbonated and Conventional Building Bricks

Prior to practical application, it is necessary to evaluate the properties of the carbonated FS-CCS brick and compare them with those of other building bricks to assess its market competitiveness. As carbonated FS-CCS brick E possesses the highest CO_2 sequestration rate, the lowest drying shrinkage and water absorption, as well as acceptable strength and soundness, it was selected as the optimal product for evaluation and comparison. Consequently, SS is identified as the optimal ferrous slag for carbonated brick production.

Table 5 compares the properties of the carbonated FS-CCS brick with the requirements for MU20 building bricks [60–62] and those of MU20 bricks available on the market. As shown in the Table 5, the carbonated brick meets or exceeds the MU20 specifications in terms of compressive strength, water absorption, and drying shrinkage, suggesting that it is a qualified MU20 brick. Moreover, comparing with other MU20 bricks, the carbonated brick exhibits acceptable strength and water absorption and the lowest drying shrinkage, indicating that it represents a competitive option in the market. Beyond these physical properties, the carbonated brick achieves a CO_2 sequestration rate of 6.44% and a SS recycling rate of 27.7%, environmental characteristics far superior to that of conventional MU20 bricks [30], making it a more sustainable alternative. Therefore, the carbonated FS-CCS brick presents a suitable and sustainable substitute for MU20 building brick in nonload-bearing and low-load-bearing applications, including partition walls, pavement blocks, curbs, and so on, offering great social, economic, and environmental benefits.

Nevertheless, this study has focused primarily on the physical properties of the carbonated brick. Its long-term durability under complex service conditions, such as sulfate attack, freeze–thaw cycles, and salt crystallization, remains to be systematically evaluated, and this constitutes an important direction for our future research.

5 | Conclusion

Based on the experiment results and the discussions presented, the following conclusion can be drawn:

1. Increasing the SS content significantly reduces the compressive strength, increases the water absorption, and impairs the soundness of the uncarbonated FS-CCS brick,

although it lowers its drying shrinkage. In contrast, the same increase in the SS content in the carbonated FS-CCS brick leads to a minor decline in compressive strength, a marginal increase in water absorption, a negligible effect on drying shrinkage, and acceptable soundness.

2. Due to the precipitation of $CaCO_3$ with a larger mole volume in the pores, the carbonation densifies the microstructure, thereby endowing the carbonated FS-CCS brick with high compressive strength and low water absorption.

3. By decomposing C–S–H with poor volume stability and precipitating $CaCO_3$ with good volume stability, carbonation mitigates the dry shrinkage of the carbonated SmS-CS mortar. Furthermore, by converting f-CaO into stable $CaCO_3$, carbonation ensures the soundness of the carbonated mortar.

4. Because SS produces less C–S–H and consumes less $Ca(OH)_2$ than GGBFS, increasing the SS content enhances the pore-filling effect during carbonation, thereby amplifying the carbonation improvement on compressive strength and water absorption. Conversely, the same increase in SS content reduces the amount of C–S–H available for decomposition, thereby attenuating the carbonation improvement on volume stability.

5. The optimal ferrous slag composition for the carbonated FS-CCS brick is 100% SS. The resulting carbonated brick demonstrate a compressive strength of 20.2 MPa, water absorption of 10.2%, drying shrinkage of 0.034%, CO_2-sequestration rate of 6.44%, and eligible soundness, meeting the MU20 building brick requirements and being superior to conventional MU20 brick due to its environmental benefits.

Funding

This work was funded by the National Key Technology R&D Program of the 11th Five-Year Plan (Grant 2006BAF02A24) and Chengdu Technological Innovation R&D Project (Grant 2026-YF05-00283-SN).

Conflicts of Interest

The authors declare no conflicts of interest.

Data Availability Statement

The data that support the findings of this study are available from the corresponding author upon reasonable request.

References

1. World Steel Committee on Economic Studies, *Steel Statistical Year Book 2023* (World Steel Association Press, 2024).

2. J.-S. L. Bernsmann and J. H. Schleifenbaum, "From Construction for Construction: Additive Manufacturing With Gas-Atomized Recycled Steel Scrap," *Circular Economy* 4, no. 3 (2025): 100157.

3. H. Liu, Y. Luo, and X. Liu, "Study on Emission Characteristics, Test and Capture Technology of CO_2 in Industrial Flue Gas," *Power Generation Technology* 45, no. 1 (2025): 62–68.

4. S. C. Pal, A. Mukherjee, and S. R. Pathak, "Investigation of Hydraulic Activity of Ground Granulated Blast Furnace Slag in Concrete," *Cement and Concrete Research* 33, no. 9 (2003): 1481–1486.

5. S. Ghorbani, Y. Sun, M. K. Mohan, and S. Matthys, "Effect of Copper and Stainless Steel Slags on Fresh, Mechanical and Pore Structure Properties of Alkali Activated Ground Granulated Blast Furnace Slag," *Case Studies in Construction Materials* 18 (2023): e01981.

6. S. Aydin and B. Baradan, "Effect of Activator Type and Content on Properties of Alkali- Activated Slag Mortars," *Composites Part B: Engineering* 57 (2014): 166–172.

7. J. Zhao, P. Yan, and D. Wang, "Research on Mineral Characteristics of Converter Steel Slag and Its Comprehensive Utilization of Internal and External Recycle," *Journal of Cleaner Production* 156 (2017): 50–61.

8. T. Zhang, Q. Yu, J. Wei, J. Li, and P. Zhang, "Preparation of High Performance Blended Cements and Reclamation of Iron Concentrate From Basic Oxygen Furnace Steel Slag," *Resources, Conservation and Recycling* 56, no. 1 (2011): 48–55.

9. C. Shi, "Steel Slag—Its Production, Processing, Characteristics, and Cementitious Properties," *Journal of Materials in Civil Engineering* 16, no. 3 (2004): 230–236.

10. W. Gao, W. Zhou, X. Lyu, X. Liu, H. Su, and C. Li, "Comprehensive Utilization of Steel Slag: A Review," *Powder Technology* 422, no. 15 (2023): 118449.

11. P. Mikhailenko, Z. Piao, and L. D. Poulikakos, "Electric Arc Furnace Slag as Aggregates in Semi-Dense Asphalt," *Case Studies in Construction Materials* 18 (2023): e02049.

12. I. Salas, P. Tamayo, E. Cifrián, C. Thomas, and A. Andrés, "Application of Electric Arc Furnace Slag in Building Concrete: Environmental and Structural Characterization," *Journal of Building Engineering* 110 (2025): 112993.

13. A. Santamaria, V. Revilla-Cuesta, M. Skaf, and J. M. Romera, "Full-Scale Sustainable Structural Concrete Containing High Proportions of By-Products and Waste," *Case Studies in Construction Materials* 18 (2023): e02142.

14. A. Aghajanian, C. Thomas, and K. Behfarina, "Effect of Micro-Silica Addition Into Electric Arc Furnace Steel Slag Eco-Efficient Concrete," *Applied Science* 11, no. 11 (2021): 4893.

15. M. Shi, Q. Wang, and Z. Zhou, "Comparison of the Properties Between High–Volume Fly Ash Concrete and High–Volume Steel Slag Concrete Under Temperature Matching Curing Condition," *Construction and Building Materials* 98 (2015): 649–655.

16. Q. Liu, J. Liu, and L. Qi, "Effects of Temperature and Carbonation Curing on the Mechanical Properties of Steel Slag-Cement Binding Materials," *Construction and Building Materials* 124 (2016): 999–1006.

17. X. Sun, J. Liu, Y. Zhao, et al., "Mechanical Activation of Steel Slag to Prepare Supplementary Cementitious Materials: A Comparative Research Based on the Particle Size Distribution, Hydration, Toxicity Assessment and Carbon Dioxide Emission," *Journal of Building Engineering* 60 (2022): 105200.

18. V. A. Nunes, P. Suraneni, A. C. S. Bezerra, C. Thomas, and P. H. R. Borges, "Influence of Activation Parameters on the Mechanical and Microstructure Properties of an Alkali-Activated BOF Steel Slag," *Applied Sciences* 12, no. 23 (2022): 12437.

19. J. Sun, Z. Zhang, S. Zhuang, and W. He, "Hydration Properties and Microstructure Characteristics of Alkali-Activated Steel Slag," *Construction and Building Materials* 241 (2020): 118141.

20. E. Adesanya, K. Ohenoja, P. Kinnunen, and M. Illikainen, "Properties and Durability of Alkali-Activated Ladle Slag," *Materials and Structure* 50, no. 6 (2017): 255.

21. M. Ozturk, M. B. Bankir, O. S. Bolukbasi, and U. K. Sevim, "Alkali Activation of Electric Arc Furnace Slag: Mechanical Properties and Micro Analyzes," *Journal of Building Engineering* 21 (2019): 97–105.

22. J. Sun and Z. Chen, "Effect of Silicate Modulus of Water Glass on the Hydration of Alkali Activated Converter Steel Slag," *Journal of Thermal Analysis and Calorimetry* 138, no. 1 (2019): 47–56.

23. C. Shi and J. Qian, "High Performance Cementing Materials From Industrial Slags—A Review," *Resources, Conservation and Recycling* 29, no. 3 (2000): 195–207.

24. R. Wang, T. Qi, H. Ji, et al., "Study on Preparation Technology and Properties of Calcium Based CO_2 Absorbent From Acid Leaching Steel Slag," *Green Energy and Resource* 3, no. 3 (2025): 100140.

25. T. Kurusta, G. Mucsi, S. Kumar, and F. Kristály, "Carbon-Dioxide Sequestration by Mechanical Activation of Linz-Donawitz Steel Slag; the Effect of Water on CO_2 Capture," *Fuel* 352 (2023): 128951.

26. C. Cheng, W. Huang, H. Xu, et al., "CO_2 Sequestration and $CaCO_3$ Recovery With Steel Slag by a Novel Two-Step Leaching and Carbonation Method," *Science of The Total Environment* 891 (2023): 164203.

27. S. N. Lekakh, C. H. Rawlins, D. G. C. Robertson, V. L. Richards, and K. D. Peaslee, "Kinetics of Aqueous Leaching and Carbonization of Steelmaking Slag," *Metallurgical and Materials Transactions B* 39, no. 1 (2008): 125–134.

28. Department of Industry Statistics, National Bureau of Statistics of China, *China Industry Statistical Yearbook* (China Statistics Press, 2024).

29. L. Zhang, "Production of Bricks From Waste Materials—A Review," *Construction and Building Materials* 47 (2013): 643–655.

30. S. Wang, L. Gainey, I. D. R. Mackinnon, et al., "Thermal Behaviors of Clay Minerals as Key Components and Additives for Fired Brick Properties: A Review," *Journal of Building Engineering* 66 (2023): 105802.

31. H. Z. Wu, J. Chang, Z. Z. Pan, and X. Cheng, "Carbonate Steelmaking Slag to Manufacture Building Materials," *Advanced Materials Research* 79–82 (2009): 1943–1946.

32. Z. Xu, Y. Zhou, and Y. Zhang, "Ultra-High Strength Carbonated Slab Prepared With Steel Slag Powders via Accelerated Carbonation for CO_2 Sequestration," *Journal of Materials Research and Technology* 24 (2023): 9058–9068.

33. G. Biava, M. Zajac, A. Principallo, L. E. Depero, M. B. Haha, and E. Bontempi, "Evaluation of Steel Slags in CO_2 Sequestration and as Supplementary Cementitious Material," *Construction and Building Materials* 489 (2025): 142271.

34. G. Liu, K. Schollbach, S. van der Laan, P. Tang, M. V. A. Florea, and H. J. H. Brouwers, "Recycling and Utilization of High Volume Converter Steel Slag Into CO_2 Activated Mortars—the Role of Slag Particle Size," *Resources, Conservation and Recycling* 160 (2020): 104883.

35. B. S. Gebregziabiher, R. Thomas, and S. Peethamparan, "Very Early-Age Reaction Kinetics and Microstructural Development in Alkali-Activated Slag," *Cement and Concrete Composite* 55 (2015): 91–102.

36. L. Li, Z. Wu, C. Hu, et al., "Performance, Hydration, and Environmental Impact of a Ternary All-Solid-Waste Binder: Roles of Ground Granulated Blast Furnace Slag, Basic Oxygen Furnace Slag, and Calcium Carbide Residue," *Powder Technology* 472 (2026): 122133.

37. R. Guo, C. Xue, Q. Li, W. Guo, H. Pan, and Q. Zhao, "Activation of Ultra-Fine Steel Slag and Ground Granulated Blast Furnace Slag in Alkaline Waste Solutions via Phosphogypsum and Calcium Carbide Slag," *Construction and Building Materials* 457 (2024): 139333.

38. W. Li and Y. Yi, "Use of Carbide Slag From Acetylene Industry for Activation of Ground Granulated Blast-Furnace Slag," *Construction and Building Materials* 238 (2020): 117713.

39. G. Zhang, D. Sun, Y. Han, et al., "Low - Alkalinity Activation of Calcium Carbide Slag for Blast Furnace Slag-Based Materials: Synergistic Effects of Carbonation Curing on Performance and Microstructure," *Journal of Building Engineering* 113 (2025): 114190.

40. Standardization Administration of the People's Republic of China, "Test Methods for Wall Bricks (GBT2542-2012)," In Chinese With English Abstract (2012).

41. Standardization Administration of the People's Republic of China, "Soundness Test Methods for Portland Cement (GB/T750-2024)," In Chinese With English Abstract (2024).

42. International Organization for Standardization, "Dense Shaped Refractory Products—Determination of Bulk Density, Apparent Porosity and True Porosity (ISO 5017-2025)," 2025, https://www.iso.org/obp/ui/en/#iso:std: 88937:en.

43. L. Mo, F. Zhang, and M. Deng, "Mechanical Performance and Microstructure of the Calcium Carbonate Binders Produced by Carbonating Steel Slag Paste Under CO_2 Curing," *Cement and Concrete Research* 88 (2016): 217–226.

44. E. Moon and Y. C. Choi, "Development of Carbon-Capture Binder Using Stainless Steel Argon Oxygen Decarburization Slag Activated by Carbonation," *Journal of Cleaner Production* 180 (2018): 642–654.

45. F. Zhang, L. Mo, and M. Deng, "Effect of Carbonation Curing on Mechanical Strength and Volume Stability of Steel Slag Concrete," *Journal of the Chinese Ceramic Society* 44, no. 5 (2016): 640–646.

46. Z. Liu, H. Zeng, and F. Wang, "Development of High Performance Carbonatable Concrete for Steel Slag Valorization," *Construction and Building Materials* 291 (2021): 123317.

47. Y. Fang, W. Su, Y. Zhang, M. Zhang, X. Ding, and Q. Wang, "Effect of Accelerated Precarbonation on Hydration Activity and Volume Stability of Steel Slag as a Supplementary Cementitious Material," *Journal of Thermal Analysis and Calorimetry* 147, no. 11 (2022): 6181–6191.

48. G. Chen, *Handbook of Mineral Thermal Analysis, Powder Crystal Analysis, and Phase Transition Spectra* (Sichuan Science and Technology Press, 1989).

49. J. E. Lyza, T. G. Fawcett, S. N. Page, and K. L. Cook, "Challenges of Quantitative Phase Analysis of Iron and Steel Slags: A Look at Sample Complexity," *Powder Diffraction* 38, no. 2 (2023): 119–138.

50. Q. Wang and P. Yan, "Hydration Properties of Basic Oxygen Furnace Steel Slag," *Construction and Building Materials* 24, no. 7 (2010): 1134–1140.

51. G. Li, P. Liu, S. Chao, et al., "The Mineral Phase Evolution Characteristics and Hydration Activity Enhancement Mechanism of Steel Slag Under NaOH Alkaline Excitation," *Journal of Alloys and Compounds* 978 (2024): 173524.

52. L. Zeng and L. Yang, "Preparation and Characterization of Ni-Doped Calcium Silicate Hydrate Based on Steel Slag: Adsorption Capacity for Rhodamine B From Aqueous Solution," *Journal of Chemistry* 2015, no. 1 (2015): 131050.

53. M. Gao, J. Wang, W. Sha, and Y. Guo, "Physico-Mechanical Properties and Synergistic Hydration Mechanism of Steel Slag-GBFS Based Alkali-Activated Composites Incorporated With Silica Fume," *Journal of Materials Research and Technology* 36 (2025): 3327–3341.

54. J. Zhao, Z. Li, D. Wang, et al., "Hydration Superposition Effect and Mechanism of Steel Slag Powder and Granulated Blast Furnace Slag Powder," *Construction and Building Materials* 366 (2023): 130101.

55. C. Zhou, X. Zhang, J. Qiao, J. Feng, and Q. Zeng, "The Deformation of C-S-H Gels and Its Link With Dynamic Length Change of Cement Pastes Upon Drying and Resaturation," *Cement and Concrete Research* 187 (2025): 107693.

56. I. Maruyama, Y. Nishioka, G. Igarashi, and K. Matsui, "Microstructural and Bulk Property Changes in Hardened Cement Paste During the First Drying Process," *Cement and Concrete Research* 58 (2014): 20–34.

57. J. A. Dean, *Lange's Handbook of Chemistry*, 13 ed. (Science Press, 1999).

58. P. A. Slegers and P. G. Rouxhet, "Carbonation of the Hydration Products of Tricalcium Silicate," *Cement and Concrete Research* 6, no. 3 (1976): 381–388.

59. C. Shi, D. Wang, F. He, and M. Liu, "Weathering Properties of CO_2-Cured Concrete Blocks," *Resources, Conservation and Recycling* 65 (2012): 11–17.

60. Standardization Administration of the People's Republic of China, "Solid Concrete Brick (GB/T21144-2023)," In Chinese With English Abstract (2023).

61. Standardization Administration of the People's Republic of China, "Fired common brick (GB5101-2017)," In Chinese With English Abstract (2017).

62. Standardization Administration of the People's Republic of China, "Non-Fired Brick With Solid Waste or Tailing (JC/T422-2025)," In Chinese With English Abstract (2025).